Bulletin of the Seismological Society of America, Vol. 99, No. 2B, pp. 1147–1161, May 2009, doi: 10.1785/0120080096

Ⓔ

Numerical Simulation of Ground Rotations along 2D Topographical Profiles under the Incidence of Elastic Plane Waves

by L. Godinho, P. Amado Mendes, A. Tadeu, A. Cadena-Isaza, C. Smerzini, F. J. Sánchez-Sesma, R. Madec, and D. Komatitsch

Abstract The surface displacement field along a topographical profile of an elastic half-space subjected to the incidence of elastic waves can be computed using different numerical methods. The method of fundamental solutions (MFS) is one of such techniques in which the diffracted field is constructed by means of a representation in terms of the Green's functions for discrete forces located outside the domain of interest. From the enforcement of boundary conditions, such forces can be computed; thus, the ground motion can be calculated. One important advantage of MFS over boundary integral techniques is that singularities are avoided. The computation of ground-motion rotations implies the application of the rotational operator to the displacement field. This can be done using either numerical derivatives or analytical expressions to compute the rotational Green's tensor. We validate the method using exact analytical solutions in terms of both displacement and rotation, which are known for simple geometries. To demonstrate the accuracy for generic geometries, we compare results against those obtained using the spectral-element method. We compute surface rotations for incoming plane waves (*P*, *SV*, and Rayleigh) near a topographical profile. We point out the effects of topography on rotational ground motion in both frequency and time domains.

Online Material: Analysis of the dependence of rotational motion on incident plane-wave frequency.

Introduction

Current seismological analysis mainly deals with amplification of translational motion caused by the seismic loads, while the rotational component of motion is still generally overlooked. In fact, it has been the standard practice in earthquake engineering and seismology to focus more on translational motion, neglecting the rotational motion around horizontal and vertical axes that occur during earthquakes.

Nevertheless, recent investigations have pointed out that rotational motions may be relevant close to the earthquake source (see, e.g., Takeo, 1998) and for surface waves (Lee and Trifunac, 1985, 1987). Based on the theory of defects, Takeo and Ito (1997) demonstrated that abrupt changes of fault slip and/or tensile fracture can generate rotational seismic waves. There are few observational evidences of how significant rotations may be in near-source regions (see, e.g., Nigbor, 1994; Takeo, 1998; Huang *et al.*, 2006). Furthermore, several studies, based partly on numerical simulations (Bouchon and Aki, 1982; Castellani and Boffi, 1986) and partly on finite-differencing of dense seismic arrays (see, e.g., Niazi, 1986; Oliveira and Bolt, 1989; Singh *et al.*, 1997; Huang, 2003; Suryanto *et al.*, 2006; Ghayamghamian and Nouri, 2007; and the recent work of Spudich and Fletcher, 2008) indicated that rotational components may be non-negligible in certain conditions. The rotational components of ground motions have also been studied theoretically, using, on one side, kinematic source models (Aki and Richards, 1980) and, on the other side, elastodynamics theory of plane wave propagation (Trifunac, 1982; Lee and Trifunac, 1985, 1987).

The potential implications of knowing rotational ground motions are basically the following:

1. In seismology, they can provide useful constraints to correct the response of the seismometers, which is polluted by rotations, even when they are expected to be very small and therefore of negligible interest from an engineering point of view. As first reviewed by Graizer (2005, 2006) and subsequently by Pillet and Virieux (2007), recovery of permanent displacement or long-period far-field wave field requires an accurate estimate of rotations. Furthermore, they might be a powerful indicator of the

local velocity structure (e.g., the presence of an alluvial basin as studied by Wang *et al.*, 2006), and in near-field regions, they might provide further constraints for the source rupture process (Takeo and Ito, 1997).

2. From an engineering standpoint, rotations may be responsible for damage in high-rise buildings and in those structures where soil-structure interaction effects are expected to be significant. For recent reviews of the potential effects of rotational ground motions on structures, we refer the reader to Trifunac (2006) and Kalkan and Graizer (2007).

However, this potential impact in seismology and the importance of rotational motion in engineering practice are still subject to debate.

An alternative approach to assess the importance of the rotational motion is to make use of numerical and mathematical models that allow the simulation of the seismic phenomena. Li *et al.* (2004) proposed a mathematical model that allows the computation of time histories of rocking motion and torsional rotation corresponding to a set of three recorded orthogonal translational components. The proposed model is based upon a representation of soil impedance and the contribution of body waves.

Classical numerical formulations based on finite differences, boundary elements, finite elements, or spectral elements have also been widely used in the simulation of seismic-wave propagation. Different approaches, mainly regarding linear motion amplification, have been used to simulate the propagation of seismic waves in the presence of topography. In particular, the spectral-element method (SEM) has been successfully used to simulate seismic-wave propagation in the presence of two- and three-dimensional (2D and 3D) topographic features (see, e.g., Komatitsch *et al.*, 1999; Paolucci *et al.*, 1999). The SEM is well suited to this problem because it is based on a variational formulation of the seismic-wave equation and is similar to the finite-element method. Therefore, the mesh can be adapted to the shape of the geometry, and the free-surface boundary condition is automatically enforced as a natural boundary condition. Pedersen *et al.* (1994) used an indirect boundary element method (BEM) formulation to calculate the 3D seismic response of 2D topographies under the incidence of plane waves using Green's functions for an infinite space. Reinoso *et al.* (1997) used a BEM formulation to compute 3D reflections by valleys and irregular topography. Later, Tadeu, Santos, and António (2001) used a direct BEM approach to compute the 3D reflected field generated in the presence of smooth topography, making use of the Green's functions for an unbounded space.

In many cases, the geometry of the problem consists of half-spaces or layered media containing inclusions; it is then possible to use fundamental solutions that take the layered structure of the medium into account without having to explicitly discretize it. One such set of functions has been proposed by Tadeu, António, and Godinho (2001) for the cases of half-spaces and solid layers subjected to 2.5D loads. The functions introduced by these authors are defined as summations of the effects of plane waves with different incidence angles with respect to the horizontal axis.

In recent years, a different class of numerical techniques has become popular: the so-called meshless techniques. A few examples are the method of fundamental solutions (MFS; Fairweather and Karageorghis, 1998; Golberg and Chen, 1999), the radial basis functions (RBF) collocation method (Kansa, 1990), and the meshless local Petrov–Galerkin method (Atluri, 2004). The MFS seems to be particularly effective in the study of wave propagation, overcoming some of the mathematical complexity of the BEM, and providing accurate solutions. Godinho *et al.* (2006) studied the performance of the MFS for simulating the propagation of acoustic waves in a fluid domain with an inclusion, concluding that the method can be very efficient, even better in terms of performance than the BEM for this type of problem. Later, Godinho *et al.* (2007) successfully applied the MFS to study acoustic and elastic wave propagation around thin structures using a domain decomposition technique.

These results indicated that the MFS should be a suitable tool to analyze the rotational motion generated in the presence of topography. We therefore develop an MFS formulation to study the rotational motion caused by the incidence of plane and surface waves in 2D geometries. First, we will present the formulation followed by a brief description of the half-space fundamental solutions used. We will then benchmark the method against known analytical solutions for specific geometrical configurations. We will also compare the results to those provided by a classical spectral-element formulation including the computation of rotations. We will then perform a number of numerical simulations to assess the magnitude of the rotational motion generated by the incidence of plane waves with different angles of incidence and by surface waves. The analyzed topographies include the classic case of a semicircular valley, triangular valleys with different slopes, elliptical canyons with different depths, and a hill. The results are analyzed in both frequency and time domains.

Generic Problem Formulation

Consider a homogeneous, linear isotropic elastic domain with mass density ρ, shear-wave velocity β, and compressional wave velocity α. In the frequency domain, the propagation of elastic waves can be described by

$$\alpha^2 \nabla(\nabla \cdot \mathbf{u}) - \beta^2 \nabla \times \nabla \times \mathbf{u} = -\omega^2 \mathbf{u}, \qquad (1)$$

where the vector $\mathbf{u}$ represents the displacement, ω is the circular frequency, and for a 3D problem, $\nabla = \frac{\partial}{\partial x}\hat{i} + \frac{\partial}{\partial y}\hat{k} + \frac{\partial}{\partial z}\hat{j}$ with $\hat{i}$, $\hat{k}$, $\hat{j}$ being unit vectors along the positive directions of

the x, y, and z axes, respectively. If the problem is purely 2D, then $\nabla = \frac{\partial}{\partial x}\hat{i} + \frac{\partial}{\partial z}\hat{j}$.

The MFS approximates the solution in terms of a linear combination of fundamental solutions of the governing equation. The approximate solution ($\underline{\hat{\mathbf{u}}}$) is then given by

$$\underline{\hat{\mathbf{u}}} = \begin{cases} \hat{u}_x = \sum_{k=1}^{N}[a_{xk}G_{xx}(x, x_k, z, z_k) \\ \qquad + a_{zk}G_{zx}(x, x_k, z, z_k)] + u_x^{\text{inc}} \\ \hat{u}_x = \sum_{k=1}^{N}[a_{xk}G_{xz}(x, x_k, z, z_k) \\ \qquad + a_{zk}G_{zz}(x, x_k, z, z_k)] + u_x^{\text{inc}} \end{cases}, \qquad (2)$$

where $\{(x_k, z_k)\}_{k=1}^{N}$ are N distinct source points on a curve that lies outside of the domain of interest, $G_{ij}(x, x_k, z, z_k)$, $(i, j = x, z)$ are the displacements in the direction j at (x, z) caused by a unit point force applied at (x_k, z_k) and directed along direction i, and u_x^{inc} and u_z^{inc} represent either an incoming plane wave or an incident field generated by a source inside of the domain. The discrete sources in equation (2) are located along a fictitious curve Γ' placed outside of the domain in order to avoid the treatment of singularities.

Once the source points have been chosen, the coefficients $\{a_{ik}\}_{k=1}^{N}$ can be determined by enforcing the boundary conditions at M collocation points along the physical boundary Γ. Here, the number of source points (N) on Γ' is typically one third of the number of collocation points (M) on boundary Γ, and the resulting equation systems are solved using a least-squares solver.

In the present work, the propagation domain consists of a half-space with a topographical feature at the surface as depicted in Figure 1, illuminated by incident elastic plane waves. The discretization of the horizontal surface of the half-space may be avoided if fundamental solutions that take its presence into account are used. For a half-space, the total wave field can be expressed by taking the incident field generated by the source (source terms) and the terms generated at the surface (surface terms) into account. The source terms can be written based on the equations proposed by Tadeu and Kausel (2000) for 2.5D loads, while the surface terms can be represented by one dilatational and two shear potentials with unknown amplitude values (Tadeu, António, and Godinho, 2001).

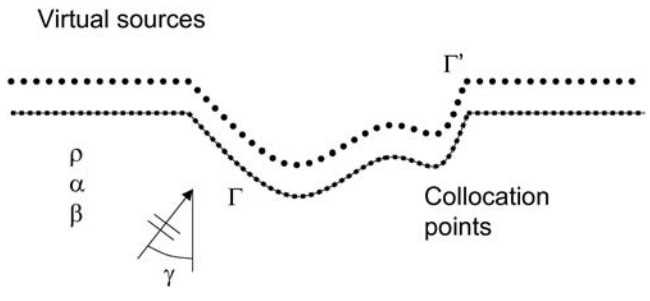

Figure 1. Geometry of the problem with the location of the sources and collocation points.

Although these fundamental solutions are accurate and easy to implement, they are computationally demanding with the involved summations requiring long computational times to reach convergence, especially when the sources or the receivers are located close to the surface of the half-space. For this reason, it can be interesting to use alternative formulations, which may result in significant improvements in terms of performance. In fact, in the alternative approach by Sánchez-Sesma and Rosenblueth (1979), the Green's function for the full-space is used for all of the fictitious sources describing the diffracted waves by the surface, while the enforcement of boundary conditions at the surface of the half-space is already included in the incident field. However, modeling the geometry using only full-space solutions implies that some additional sources and collocation points have to be considered along the surface of the half-space near the geometric discontinuity. The distance to be discretized on each side of the discontinuity should be large enough so that all relevant contributions from surface reflections are taken into account and spurious wave arrivals will not interfere with the response recorded at the receivers. In this work, we consider a distance equal to five times the length of the topographical feature on each side, along which the additional sources and collocation points should be placed. A graphical representation of the model is shown in Figure 1.

The fundamental solutions to be used are thus simple and can be written as (see Sánchez-Sesma and Campillo, 1991; Tadeu and Kausel, 2000)

$$\begin{aligned} &G_{ij}(x, x_k, z, z_k) = -\frac{i}{8\rho}[(A + B)\delta_{ij} - 2B\gamma_i\gamma_j], \\ &\text{with} \quad A = \frac{H_0^{(2)}(k_\alpha r)}{\alpha^2} + \frac{H_0^{(2)}(k_\beta r)}{\beta^2}, \qquad k_\alpha = \frac{\omega}{\alpha}, \\ &\text{and} \quad k_\beta = \frac{\omega}{\beta}, \qquad B = \frac{H_2^{(2)}(k_\alpha r)}{\alpha^2} - \frac{H_2^{(2)}(k_\beta r)}{\beta^2}, \\ &\qquad \gamma_i = \partial r/\partial x_i, \qquad \gamma_j = \partial r/\partial x_j, \end{aligned} \qquad (3)$$

where $r = \sqrt{(x - x_0)^2 + (y - y_0)^2}$ ($[x_0, y_0]$ being the position of the source).

The rotational motion can be computed by analytically calculating the necessary derivatives of these functions to obtain $\theta_y = -\frac{1}{2}(\frac{\partial \hat{u}_x}{\partial z} - \frac{\partial \hat{u}_z}{\partial x})$. Applying this operator to the aforementioned defined fundamental solutions, the rotational field can be expressed as

$$\theta_y = \frac{i}{8\mu} k_\beta H_1^{(2)}(k_\beta r)(\gamma_j\phi_i - \gamma_i\phi_j), \qquad (4)$$

where $\phi_i$is the ith component of the applied unit force.

As for the incident field, different types of waves may be taken into account. Defining the apparent horizontal wave velocity, c, and the wavenumbers $l = \frac{\omega}{c}$, $m = \sqrt{(\frac{\omega}{\alpha})^2 - l^2}$,

and $k = \sqrt{\left(\frac{\omega}{\beta}\right)^2 - l^2}$ for the case of incident P and SV waves, the wave field generated in the presence of a half-space can be written as a function of one dilatational (ϕ_1) and one shear (ψ_1) potential,

$$\begin{aligned} \phi_1 &= (A_1 e^{imz} + A_2 e^{-imz}) e^{-ilx}, \\ \psi_1 &= (B_1 e^{ikz} + B_2 e^{-ikz}) e^{-ilx}, \end{aligned} \tag{5}$$

in which A_1 and B_1 represent the amplitude of the incident P and SV waves, respectively, and A_2 and B_2 are unknown coefficients to be determined by enforcing the fact that the traction vector vanishes along the free surface. The rotational motion generated at the surface of an elastic half-space can then be written as

$$\theta_y^{(0)} = -\frac{1}{2}(k^2 + l^2)\psi_1. \tag{6}$$

Model Verification

The previously defined MFS model was first applied to a number of test cases, comparing the results it provides with those computed by applying other techniques. In what follows, we present a number of results from those tests.

Verification against Analytical Solutions—The Case of a Wedge

When the geometric configuration of the topographical profile is that of a wedge with an internal angle of 120° (Fig. 2a), and the propagation medium has a Poisson ratio $\nu = 0.25$, it becomes possible to analytically calculate the solution for the displacement field when the system is illuminated by an incident SV-plane wave with an incident angle $\gamma = 0°$ as shown by Sánchez-Sesma (1990). For this case, adequately differentiating the displacements, the rotational motion can be obtained as

$$\theta_y = -u_0 k e^{-ikh} \sin[k(z + h)], \tag{7}$$

where u_0 is the incident displacement field, and h is the depth of the wedge structure as identified in Figure 2a.

We analyzed this geometry using the MFS model with a number of collocation points ranging from 5 to 20 per wavelength. Observation of the results allowed us to conclude that they approach the analytical solution as a higher number of points is considered. However, very small differences were found between the results above 15 points per wavelength. Thus, the presented results are computed using 15 collocation points per wavelength for the different frequencies of the incident wave. Figure 2b shows the corresponding results (numerical and analytical) for the dimensionless frequency $\eta = \frac{\omega a}{\beta \pi}$, where a is half the width of the irregularity. The presented displacements are normalized with respect to the incident field u_0, while the normalized rotations are obtained as $\frac{\theta_y a}{u_0 \eta}$. Observing these results, we conclude that the MFS provides a very accurate estimation of both the displacements and the rotation.

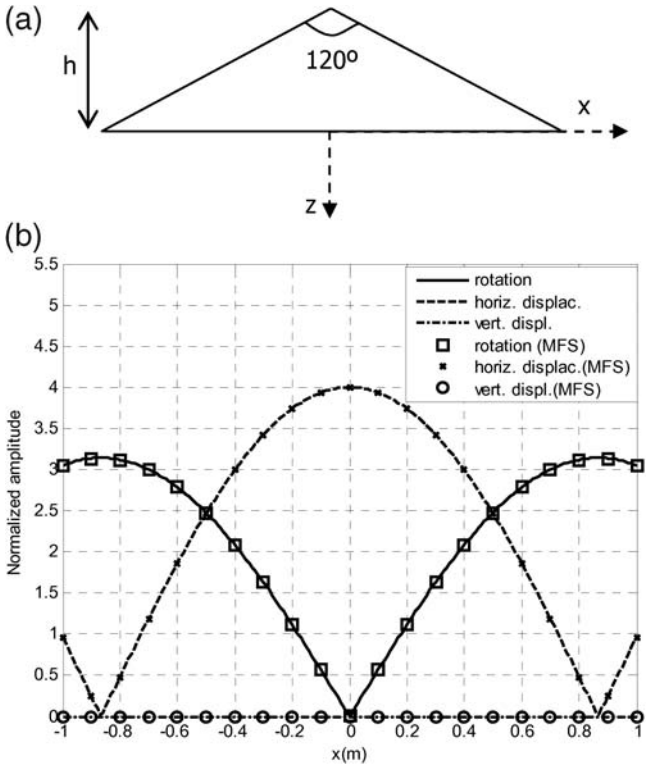

Figure 2. (a) Geometry of the topography used in the verification. (b) Normalized displacements and rotations at the surface.

Benchmarks for Generic Geometries

To ensure that reliable results are obtained, we benchmark the proposed MFS against an SEM for a few simple geometrical configurations. As previously mentioned, the spectral-element method is an independent numerical technique similar to the finite-element method that has been extensively validated and used to study 2D and 3D seismic-wave propagation problems in recent years (see, e.g., Komatitsch *et al.*, 2005 for a review and references therein).

By running this method, we obtain two seismograms composed of seismic traces in the time domain for the two components of the 2D displacement vector. We perform a Fourier transform of each trace to measure spectral amplitude at a given normalized frequency η, and then the SEM results can be compared with the MFS results, which are obtained in the frequency domain. To introduce initial plane waves in the SEM mesh, the displacement field is split into an incident field in a half-space and a diffracted field resulting from the presence of topography at the free surface of the half-space. The incident field in the half-space is analytically known;

therefore, its exact expression is implemented in the SEM code, whereas the diffracted field is numerically computed by the SEM. To simulate a semi-infinite half-space, absorbing conditions are implemented on all of the boundaries of the mesh except the free surface based on the method of Bielak and Christiano (1984), in which the known initial field is subtracted on the boundary during propagation; then, one only needs to absorb the diffracted wave field.

The first set of results corresponds to the case of a semi-circular canyon, as depicted in Figure 3, subjected to a plane *P* or *SV* wave with a 60° incidence angle. Both translational (along the x and z axes) and rotational motions are computed. Figures 4 and 5 present the results computed along a line of receivers located exactly at the surface when the incident wave field has a normalized frequency $\eta = 1$. The medium has a Poisson ratio of 0.25. The SEM calculation is performed on a mesh of 4000 spectral elements with five Gauss–Lobatto–Legendre points in each direction of each element. Therefore, we have a total of 64,681 unique grid points in the global mesh. We take a timestep $\Delta t = 0.001$ sec in the explicit and conditionally stable time-evolution scheme; therefore, for the mesh of Figure 3, we experimentally measure a Courant–Friedrichs–Lewy (CFL) stability number $\alpha \Delta t / \Delta x = 0.255$ (the upper limit found by trial and error is around 0.45). We let the calculation run for a total duration of 12 sec.

The SEM and MFS results are in good agreement, which indicates a good behavior of the MFS for the analyzed problem.

Let us perform a second benchmark for another topographic profile, the Gaussian-shaped hill represented in Figure 6. We study the response of that hill under the incidence of a Rayleigh wave based on both the MFS and the SEM. Figure 7 shows the results computed along a line of receivers located exactly at the free surface. The SEM calculation is performed on a mesh of 4000 deformed quadrangles adapted to the shape of the hill. Each quadrangle is defined by nine control points in order to have curved boundaries that can better fit the topography. We use five Gauss–Lobatto–Legendre points in each direction for each element; therefore, we have a total of 64,561 unique grid points in the mesh. We take a timestep $\Delta t = 0.04$ sec, that is, a CFL stability number of 0.223. We let the calculation run for a total duration of 12 sec.

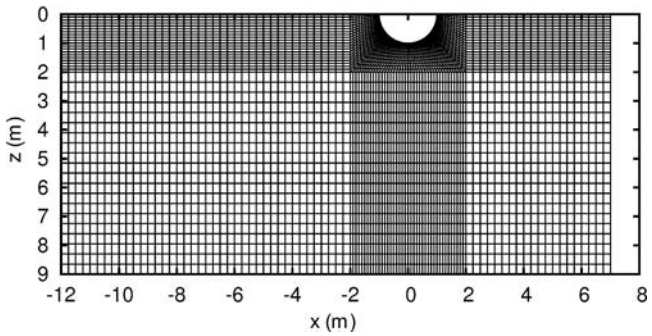

Figure 3. Mesh used in the spectral-element method to describe the geometry of the canyon model.

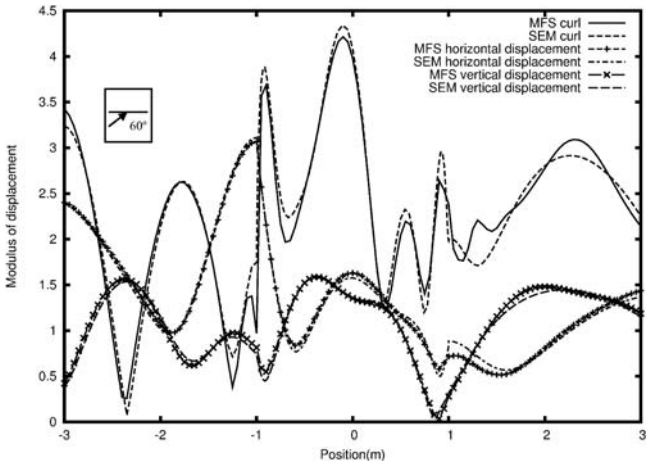

Figure 4. Comparison between the spectral amplitude computed based on the SEM and based on the MFS for the rotational, horizontal, and vertical components of displacement in the case of a *P* wave with an incidence angle of 60°.

In Figure 7a, results obtained for a specific normalized frequency of $\eta = 1.0$ are displayed, showing a good agreement, although small differences are observed between the two curves. To make sure that these differences are not significant, synthetic seismograms have also been computed considering an incident Rayleigh wave defined by a Ricker pulse with a characteristic period $T = 4$ and a delay of 6. A normalized time scale is used, with the normalized time being given by $\bar{t} = t \times \frac{\beta}{a}$, where a is half of the width of the irregularity and β is the *S*-wave velocity. The results pre-

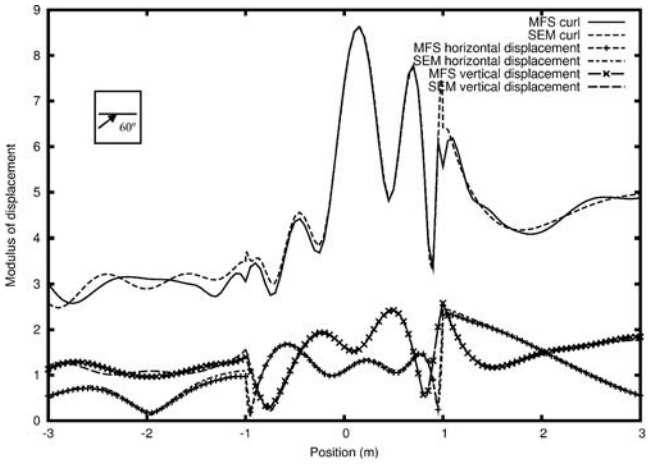

Figure 5. Comparison between the spectral amplitude computed based on the SEM and based on the MFS for the rotational, horizontal, and vertical components of displacement in the case of an *SV* wave with an incidence angle of 60°.

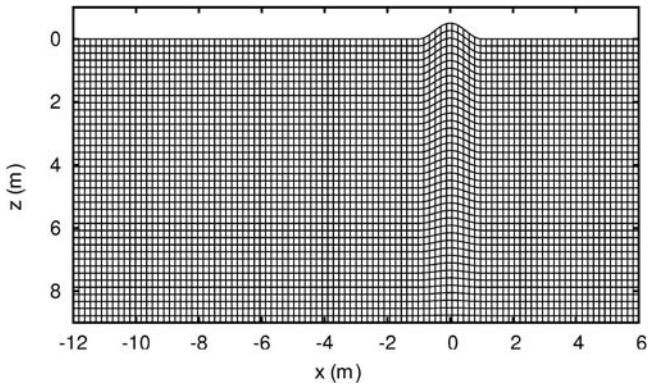

Figure 6. Mesh used in the spectral-element method to describe the geometry of the hill model.

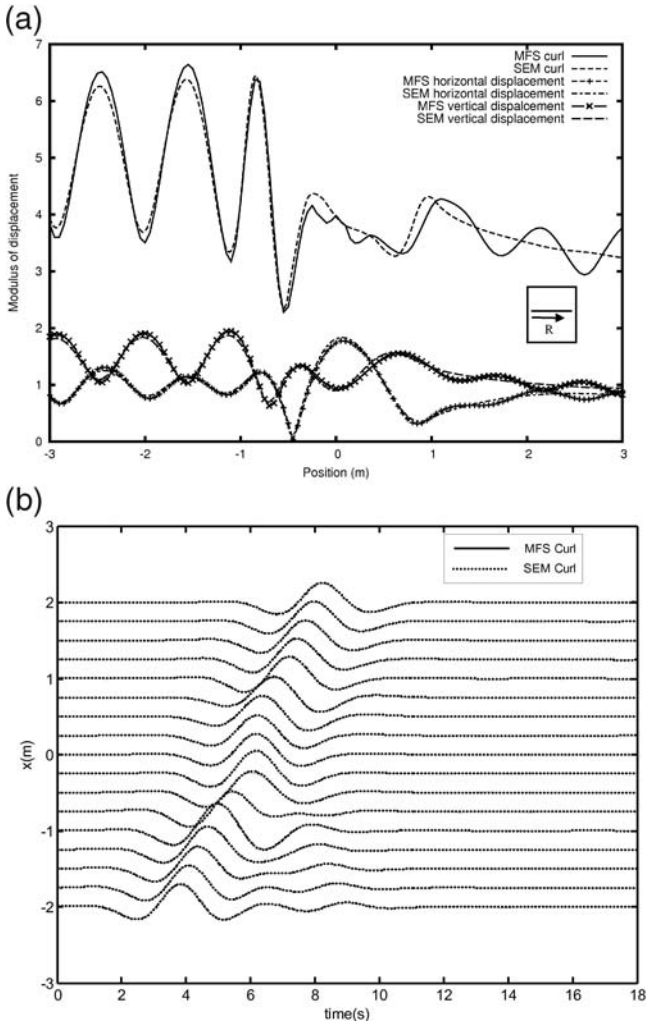

Figure 7. Verification results for the case of an incident Rayleigh wave: (a) comparison between the spectral amplitude computed using the SEM and the MFS for the rotational, horizontal, and vertical components of displacement and (b) comparison of synthetic seismograms for rotational motion, computed by the SEM and MFS at 17 stations located along the surface.

sented in Figure 7b show that there is an excellent agreement between the seismograms computed by both methods.

Influence of Surface Topography on the Rotational Motion

Although earthquake-induced translational ground motions have been widely studied, the knowledge on the corresponding rotational components and on their possible dependence on topographical irregularity is still very limited. In this section, a number of 2D typical topographical configurations, subject to the incidence of different wave types, is analyzed using the proposed MFS method.

To ensure that comparable results are obtained between all of the presented cases, the problem is normalized with respect to half of the horizontal dimension of the irregularity (a); a constant Poisson ratio $\nu = 0.25$ is assumed throughout this section. For this reason, results in the frequency domain are shown as a function of the dimensionless frequency $\eta = \frac{\omega}{\beta}\frac{a}{\pi}$. As a reference, the results for an elastic half-space were first calculated for $\eta = 1$ and are presented in Figure 8a,b for incident P and SV waves with different incidence angles, respectively. For both cases, the figures display the displacements normalized with respect to the incident field and the normalized rotations given by $\frac{\theta_y a}{u_0 \eta}$. As expected, when the incident wave is a P wave, the maximum vertical displacement is recorded for an incidence angle of 0°, while zero displacement is recorded for 90° incidence. Globally, these results seem to be consistent with those presented by Trifunac (1982). When the incident field is given by SV waves, the response is significantly different, but the displacements in both vertical and horizontal directions still follow the results presented by Trifunac. The rotations generated at the surface vary somewhat differently, reaching maximum values for different incidence angles γ. Although a systematic correlation between translational and rotation ground motions is not found, vertical displacements and rotations show similar patterns.

When a surface irregularity is introduced (see Fig. 9), the generated wave field becomes more complicated. Figure 10 depicts some representative results for the case of a semicircular canyon (defined by the geometry displayed in Fig. 9 with $a = 1$ m and $d = 1$ m) under the incidence of both P and SV waves. For simplicity, only the case of a normalized frequency $\eta = 1$ will be discussed herein. In all cases, the geometries have been described using a number of collocation points at the surface, large enough to ensure a minimum of 15 points per wavelength λ.

It is worth noticing that marked discontinuities occur at the edges of the canyon. Although these discontinuities are more visible in the rotational response, they can also be seen in the vertical and horizontal displacements; they may be associated with the sharp edge that exists at this point. For lower inclinations of the incident plane wave, peak values of the rotation are recorded near this edge as can be seen in

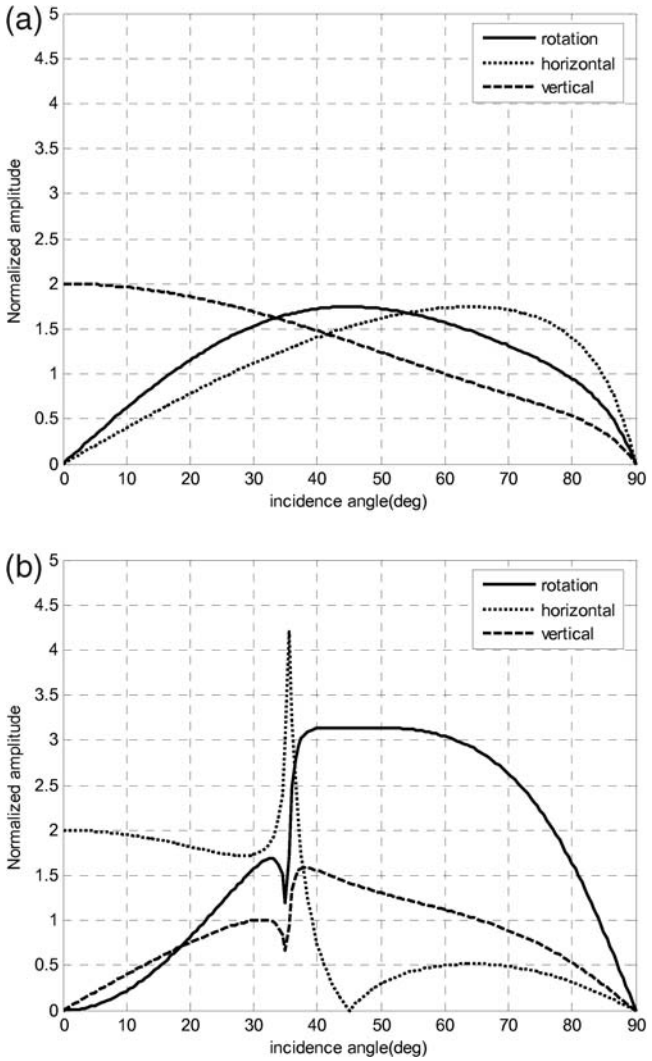

Figure 8. Results for an elastic half-space under the incidence of (a) *P* waves and (b) *SV* waves.

Figure 10a,b for incident *P* and *SV* waves parallel to the surface. However, as γ approaches larger values, high amplifications are recorded at the central part of the irregularity, reaching normalized rotations of amplitude 9 for *SV* waves with $\gamma = 60°$. Comparing the incidence of *P* and *SV* waves, it can be seen that the rotational motion generated by the latter are much larger, as intuitively expected by simple theoretical considerations (e.g., Cochard *et al.*, 2006).

Although no results are presented for other frequencies, a systematic study has been conducted analyzing the relation of both displacements and rotations with frequency. In this analysis (Ⓔsee the electronic edition of *BSSA*), it was found that, as a general tendency, a similar behavior is obtained, but the responses tend to exhibit a more pronounced oscillatory behavior; the influence of the topographical feature is further enhanced with respect to the case $\eta = 1$.

It is important to note that, although all results for rotational motion in Figure 10 are presented as normalized rotations, these results can be easily related to relevant physical quantities and may be used to predict rotational motion amplifications for more specific conditions. Consider, for instance, that the incident wave is generated in the context by an M_w 6 earthquake generated by a fault rupture at a depth of 4 km and that the propagation medium at the surface has an *S*-wave velocity of 1000 m/sec. Using the well-known attenuation law proposed by Joyner and Boore (1993), it is possible to assess the particle velocity for such incoming waves by means of

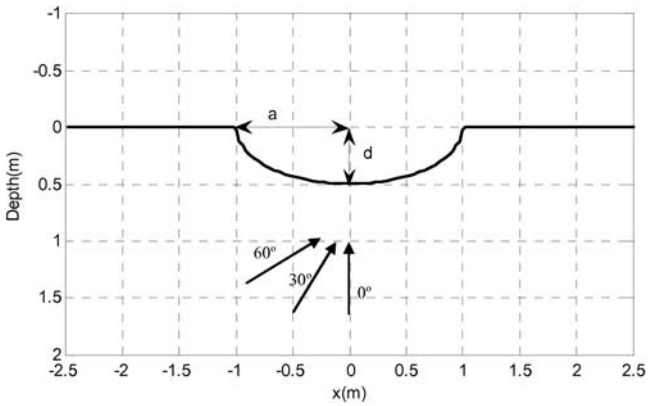

Figure 9. Geometry of the elliptical canyon.

$$\log_{10}(v) = 2.150 + 0.461 \times (M_w - 6) - \log_{10}\left(\sqrt{R^2 + 4^2}\right) - 0.00256 \times \left(\sqrt{R^2 + 4^2}\right) + 0.167, \quad (8)$$

where R is the distance from the station to the projection of the fault rupture surface on the earth surface and M_w is the moment magnitude. Using this expression, we can conclude that this earthquake would generate velocities around 18 cm/sec at $R = 10$ km and 0.57 cm/sec for $R = 150$ km. Because the normalized rotation can be written as $\frac{\theta_y \beta \pi}{v_0}$, a unit normalized rotation implies a rotational motion of 0.6×10^{-4} rad in the first case and of 1.8×10^{-6} rad in the second. From the amplifications displayed in Figure 10c for an incoming *SV* wave, it is possible to establish that the peak rotational motions predicted for the epicentral region would be of about 5.4×10^{-4} rad. This value is large enough to induce significant structural damage and even failure. However, the precise understanding of the rotational structural vulnerability contributing factors (damping, ductility, dominant period, etc.) will require more data and further scrutiny.

To give insight into the physics behind the performed simulations, time domain results are also computed. To this end, the synthetic seismograms have been computed from the corresponding transfer functions calculated for $N = 128$ frequencies by means of an inverse Fourier transform, assuming that the incident wave corresponds to a Ricker pulse

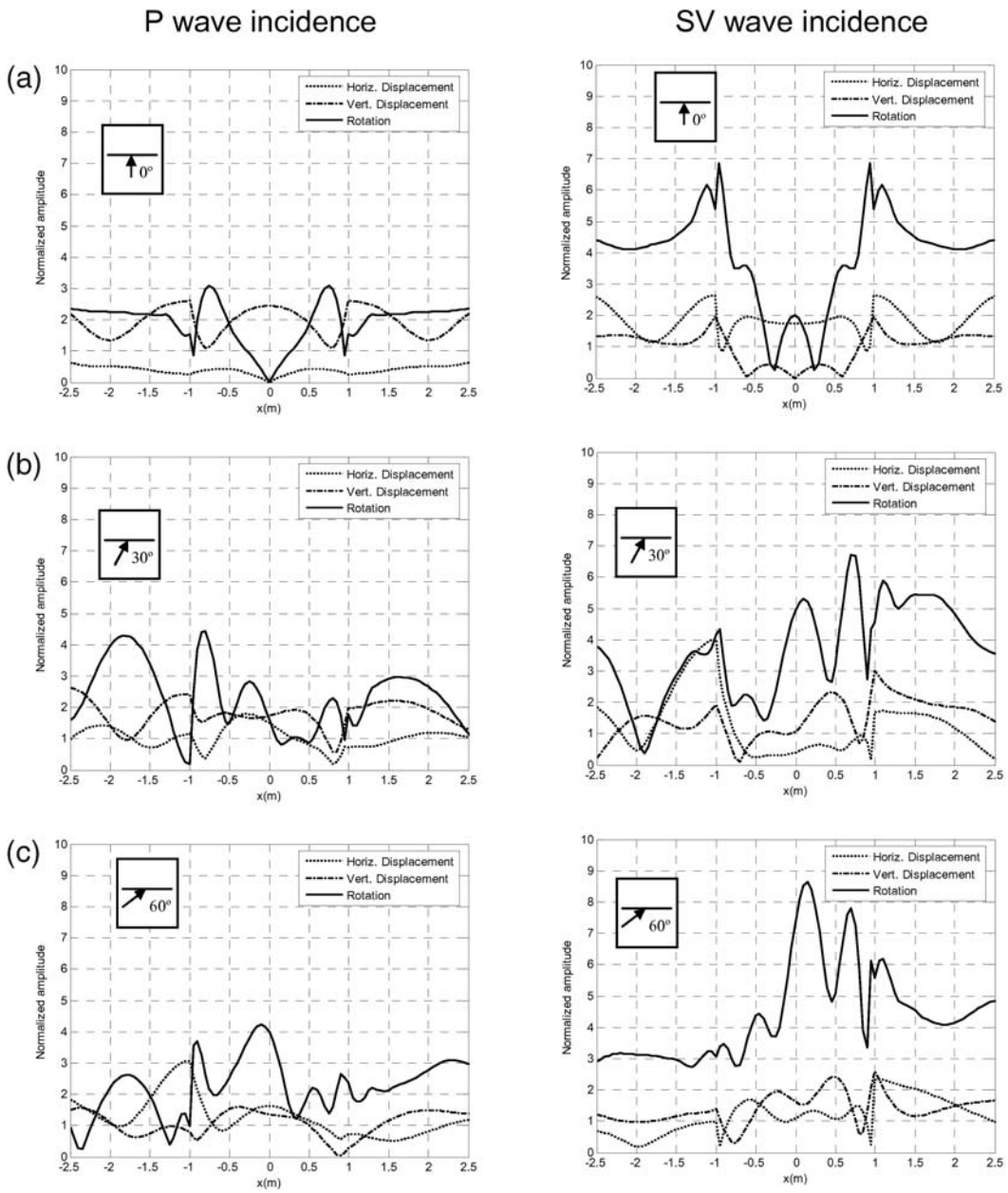

Figure 10. Results for a semicircular canyon ($d = 1$ m): incidence at (a) 0°, (b) 30°, and (c) 60°.

with a characteristic period $T = 2$ and a delay of 6. Time signals are displayed in Figure 11 in terms of horizontal displacement (left), vertical displacement (center), and rotation (right) using a normalized time scale such that $\bar{t} = t \times \frac{\beta}{a}$. Observing this figure, it is possible to confirm that no rotations are generated by an incident P wave; thus, these rotational effects can only be observed once the incident pulse impinges upon the surface. Globally, the rotational ground response at the surface exhibits similar patterns to those of the displacement field. However, under the incidence of SV waves, rotational ground motions seem to be more significant, which is consistent with what is observed in the frequency domain.

The relative depth of the canyon can also have significant effects on the surface ground response. To assess its importance, parametric analyses with respect to the parameter d have been carried out. In Figure 12, results for incident SV waves at 30° and 60° are shown for elliptical canyons with $d = 0.25$, 0.5, and 0.75 m. The response for $d = 0.25$ m appears more regular with flatter curves describing the displacement field at the surface points. However, a marked amplification in the rotational response is still recorded at the edge of the irregularity located at $x = 1.0$ m when the incidence angle is 60°. Observing the results for the other two geometries, it can be seen that, in fact, at this point a marked amplification is always recorded; this is the region where

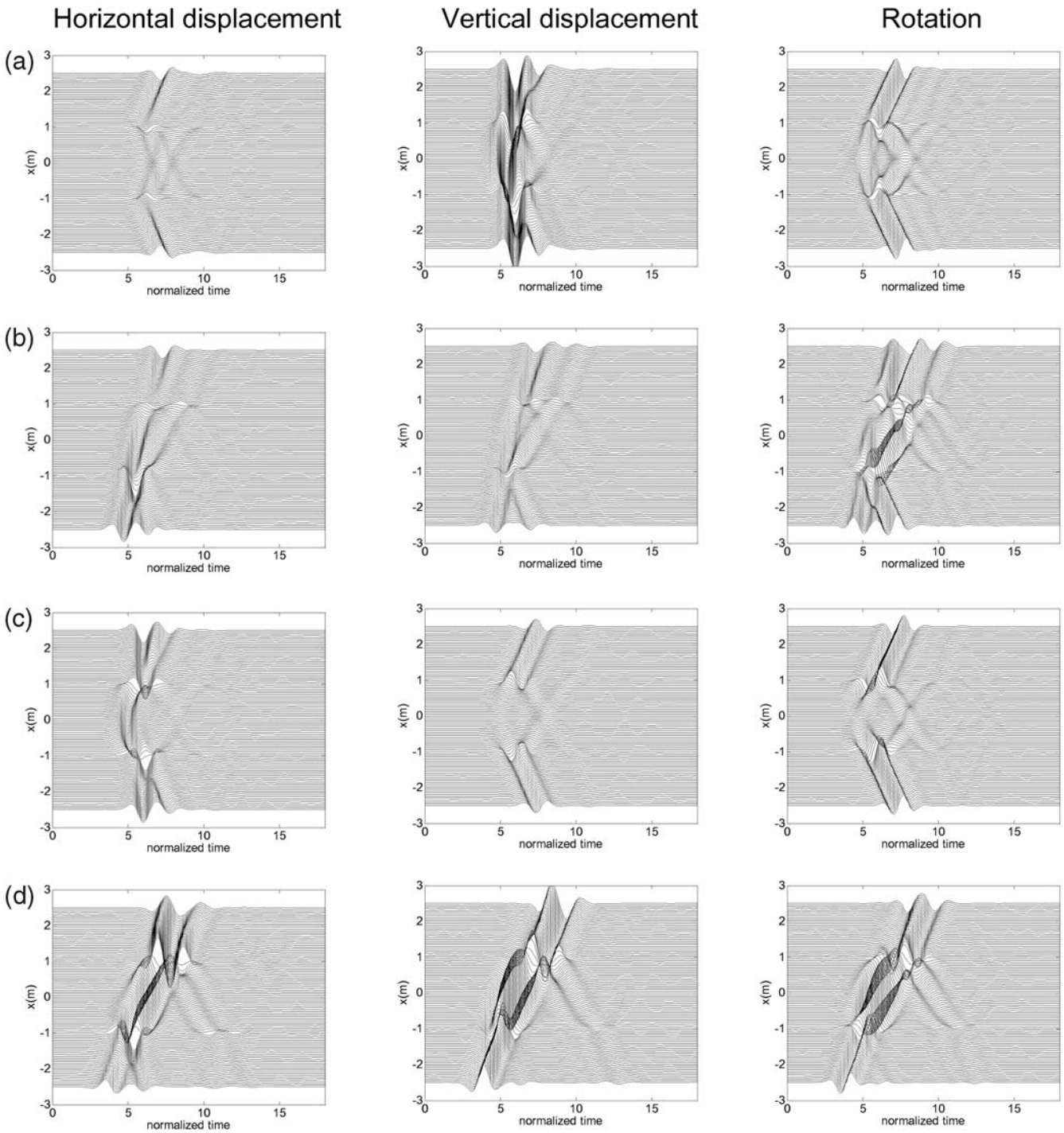

Figure 11. Normalized time signals for a semicircular canyon ($d = 1$ m) under the incidence of (a) *P* wave at 0°, (b) *P* wave at 60°, (c) *SV* wave at 0°, and (d) *SV* wave at 60°.

peak values occur. By contrast, in all cases, rotations around $x = 0.5$ m are minimum. As a general trend, amplification of surface ground motions tends to occur in the ascending part of the canyon ($x > 0$ m), while deamplification can be observed in the descending part ($x < 0$ m). It is possible to observe that, globally, as larger values of d are considered, larger amplifications occur. Interestingly, for all cases, the amplification of the rotational field is more pronounced than that of the translational field. However, there seems to be a limit for this amplification, which is generally not exceeded in the normalized rotational response. In fact, although marked amplifications have been identified in Figures 10 and 12, the normalized rotation is generally lower than 2π. Because the presented results are normalized with

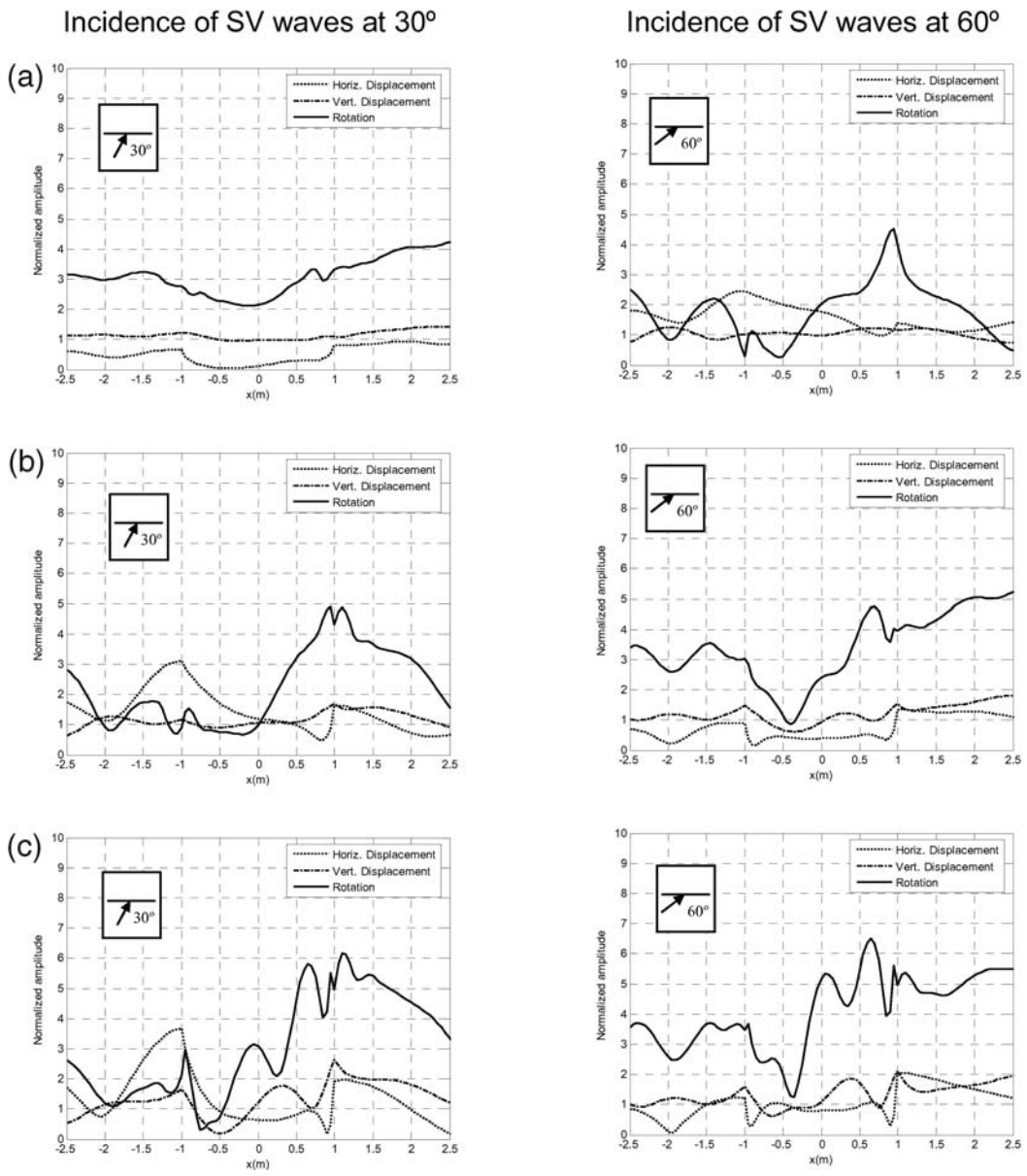

Figure 12. Results for the elliptical canyon with different depths: (a) $d = 0.25$ m, (b) $d = 0.50$ m, and (c) $d = 0.75$ m.

respect to the incident displacement field and to the dimensionless frequency, the rotational motion should follow the relation

$$\theta_y \leq 2\pi u_0 \eta = 2u_0 \frac{\omega\, a}{\beta}. \tag{9}$$

Analyzing the previous equation, we believe that, in general, the rotations scale with the ground velocity and should be bounded by the upper limit $\dot{u}_g/\beta$. However, localized amplification due to diffraction effects may generate local peaks as can be seen in Figure 10c for the incidence of *SV* waves at 60°.

After acquiring confidence with rotational ground motions induced by smooth topographies, the influence of sharp geometric irregularities is investigated. In fact, it is known that the presence of sharp edges significantly influences the propagation of seismic waves; thus, it may influence both the displacements and the rotations recorded at the surface. For this purpose, a number of simulations was performed for triangular canyons with varying depths (see Fig. 13). Figure 14 displays the results computed for two different values of the canyon depth when the incidence of *SV* waves occurs at 0°, 30°, and 60°.

As expected, the amplification of both displacements and rotations decreases as lower depths are considered; the displacements' and rotations' curves have a smoother trend. For 0° incidence, the recorded response is symmetric, and peak amplifications are visible after the transition from the

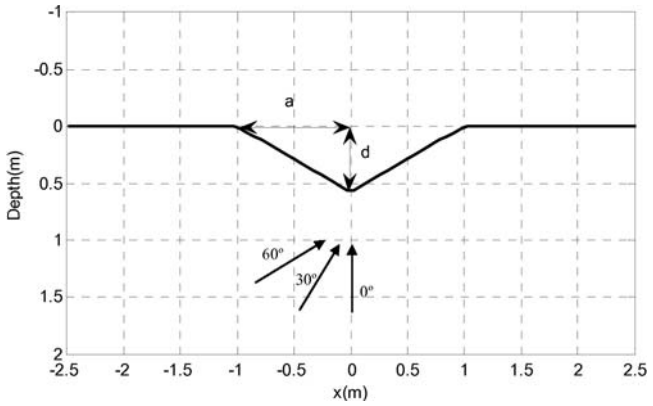

Figure 13. Geometry of the triangular canyon.

half-space to the canyon. As higher incidence angles are considered, the response becomes more complex, and, as in the previous examples, an amplified rotational response is visible in the ascending part of the topographic feature (between $x = 0.0$ m and $x = 1.0$ m). Interestingly, the displacement field in this region exhibits very little amplification, indicating that the rotational effects are stronger than the translational ones. Again, it is worth noting that the normalized rotations do not exceed 2π, following the relation defined in equation (9).

A particular case of seismic-wave incidence occurs when Rayleigh waves are generated because these waves have an important rotational component themselves. The in-

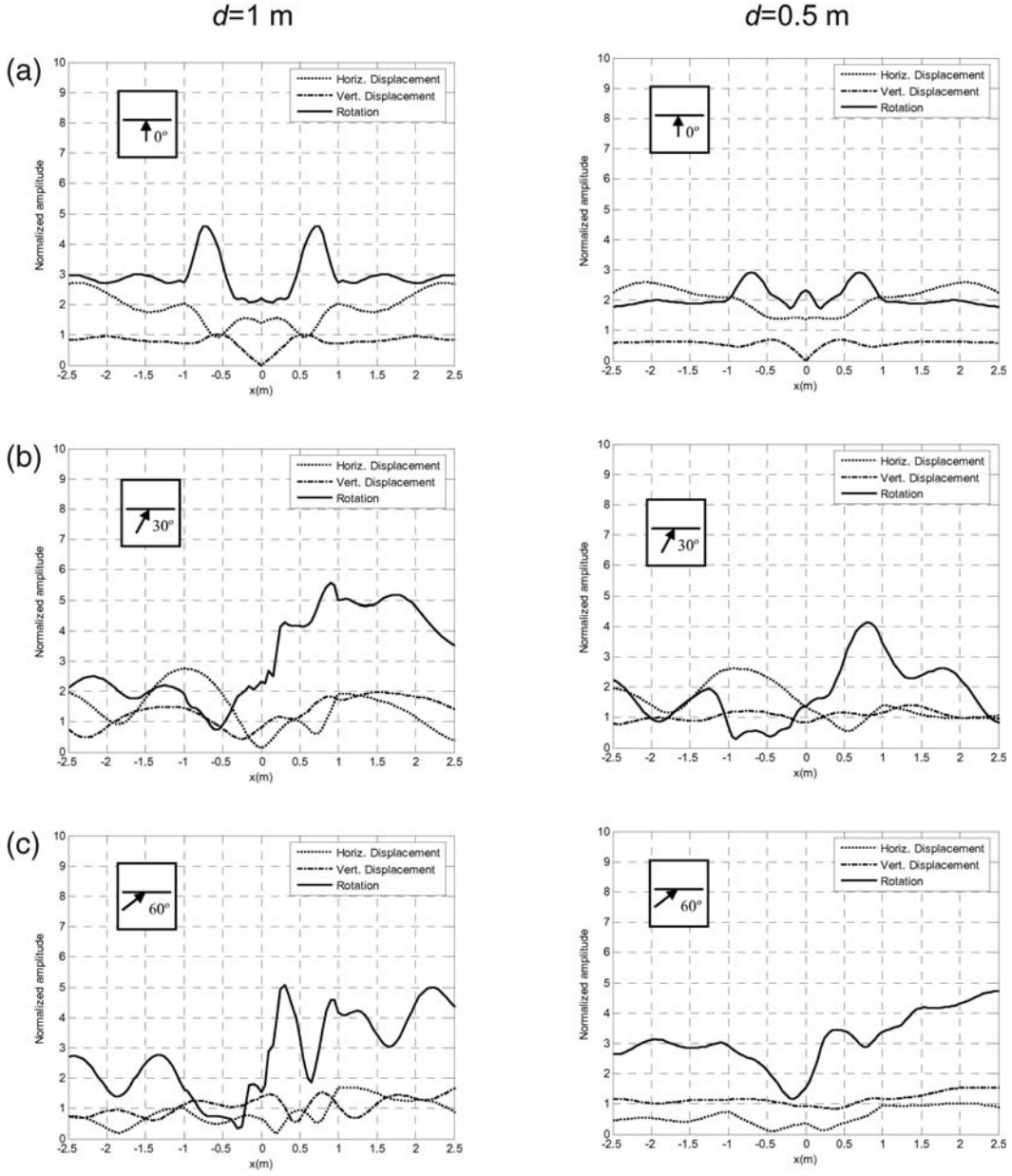

Figure 14. Results for triangular canyons under the incidence of an *SV* wave: incidence at (a) 0°, (b) 30°, and (c) 60°.

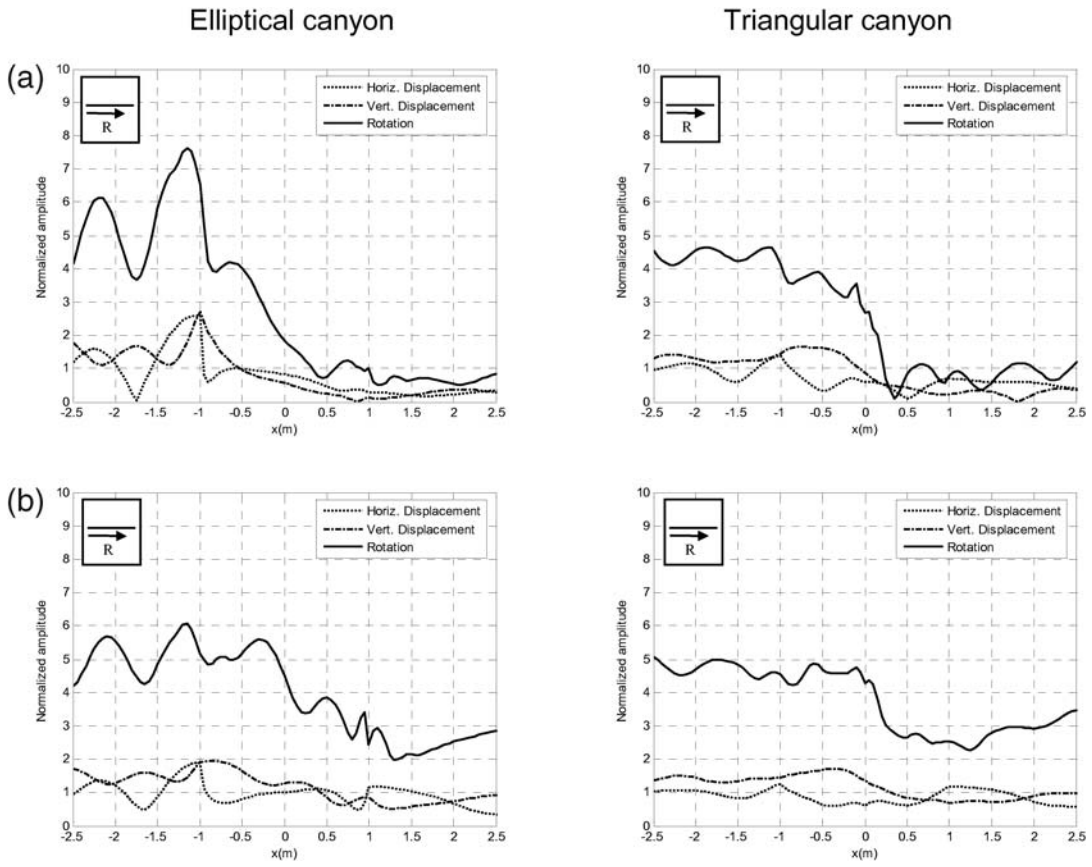

Figure 15. Results for different canyon geometries under the incidence of a Rayleigh wave: (a) $d = 1.0$ m and (b) $d = 0.5$ m.

cidence of Rayleigh waves has also been simulated; the results computed for elliptical and for triangular canyons with different depths are displayed in Figure 15.

The results obtained for this type of incidence reveal similar behaviors for the two geometries with the canyon attenuating both the rotational and the translational response. Indeed, both cases register responses close to those of the half-space (Fig. 16) before the canyon ($x \leq 1.0$ m), and then a progressive decrease occurs as the receiver points are placed further away from the source region. Once again, the relation defined by equation (9) seems to be generally followed with the exception of very localized amplifications occurring near the edge of the elliptical canyon.

It is interesting to note that the energy of the displacement and rotation field smoothly decreases when the canyon has rounded geometry, while a steep decrease is visible right after the edge of the triangular canyon. This behavior indicates a very strong diffraction effect that may be occurring at the edge of the triangular canyon, which helps to spread the energy of the propagating wave throughout the propagation domain.

The previously described behaviors can be further confirmed in the time domain plots presented in Figure 17, computed for an incident Rayleigh wave defined by a Ricker pulse with a characteristic period $T = 4$ and a delay of 6. In this figure, the time responses generated by the incidence of a Rayleigh wave in the presence of elliptical canyons with $d = 1.0$ m and with $d = 0.5$ m are displayed, together with the response generated in the presence of a triangular canyon

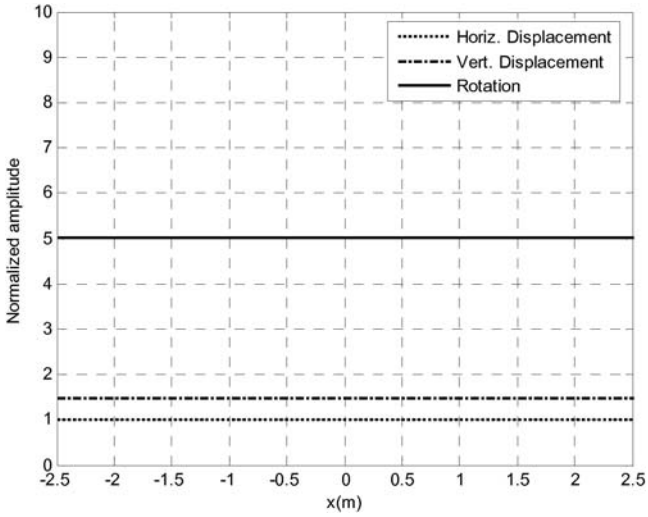

Figure 16. Displacements and rotations for a half-space under the incidence of a Rayleigh wave.

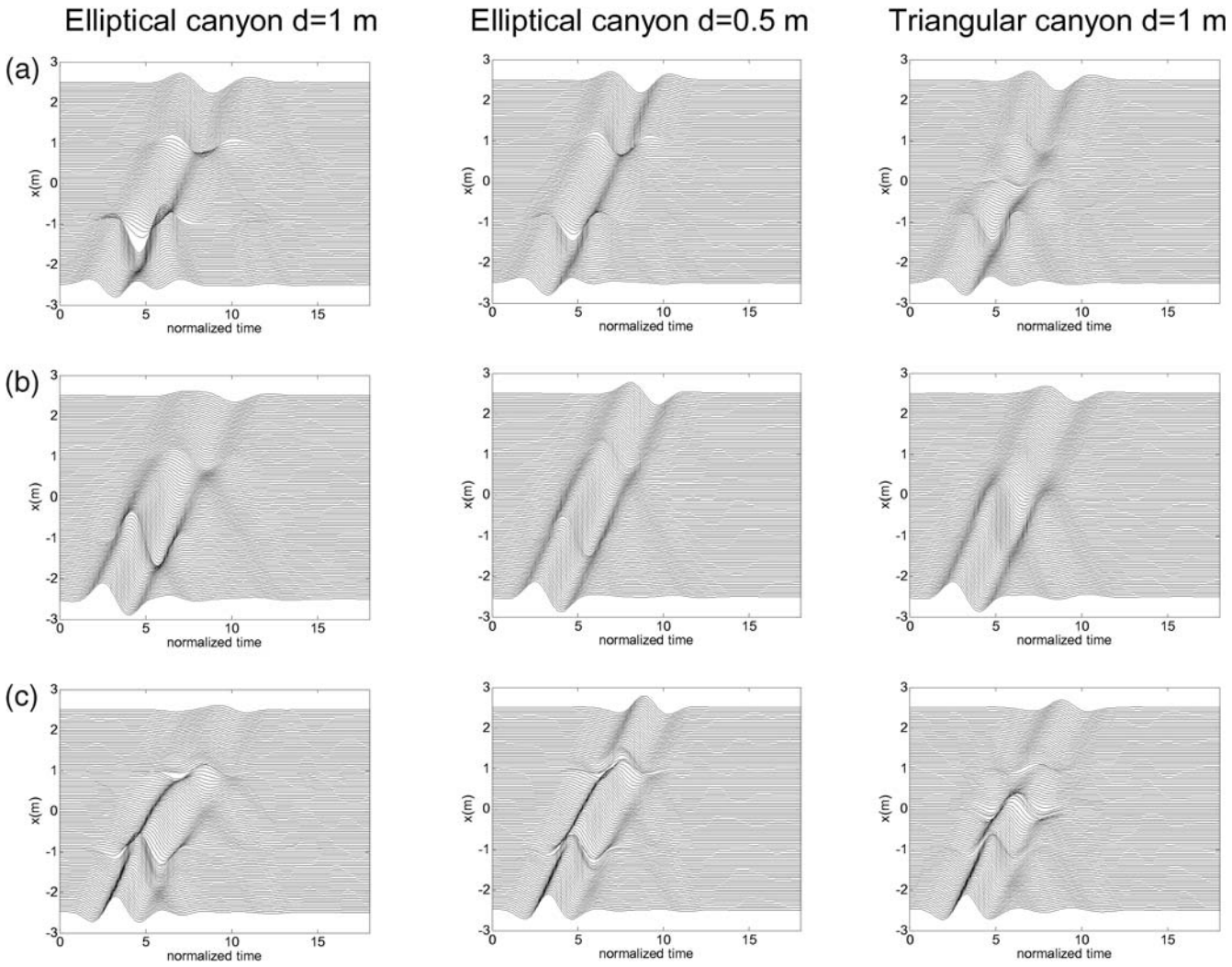

Figure 17. Normalized time domain responses along the surface of canyons with different geometries under the incidence of a Rayleigh wave: (a) horizontal displacement, (b) vertical displacement, and (c) rotation.

with $d = 1.0$ m. It is apparent that there is a smoother variation in the amplitude when the canyon has a smoother shape with the energy being slowly transferred to the propagation domain along the curve defining the canyon. It is possible to observe that the rotational motion follows a pattern similar to that of the displacements with the shield effect of the canyon being clearly visible in the upper half of these plots. It is also clear that the vertex in the triangular canyon has a very strong effect in the response, which is even more evident in the rotational field. For this case, the position of the vertex can be easily identified from the marked deamplification occurring at this specific point.

Conclusions

In this article, we evaluated the rotational ground motion at the surface of a 2D half-space with a topographical profile using an MFS method, which was verified using both analytical solutions known for wedges with specific internal angles and the SEM, which is applicable to arbitrary geometries. The method provided stable and accurate results and proved to be adequate for the study of rotational motion.

We then analyzed different topographical features, namely, elliptical and triangular canyons of varying depths under the incidence of *P*, *SV*, and Rayleigh waves. For all cases, significant amplifications were found in both the rotational and the translational fields. As inferred from previous theoretical studies, a comparative analysis revealed that larger amplifications of the rotational motion at the surface are generated by *SV* and Rayleigh waves. The computed results confirmed that the shape and depth of the canyon are important variables that influence the level of amplification and deamplification recorded at the surface. The shield effect of canyons for displacements under oblique incidence of plane waves and Rayleigh surface waves is also clearly identifiable for rotations. For all cases, time responses reveal

a very strong contribution of *SV* and Rayleigh waves, which are a dominant factor for the rotational motion.

From the various cases studied in this work, we believe that rotational ground motion should be generally bounded by the expected (or nominal) ground velocity divided by the shear-wave propagation velocity. As a general guideline, ground rotations scale with ground-motion velocities; however, diffraction may induce significant localized variations. More specific guidelines will emerge after the analysis of real data using more powerful methods that consider realistic models of surface geology.

Data and Resources

All data used in this article came from published sources listed in the references.

Acknowledgments

This work stems from the International Workshop on Rotational Seismology held at Menlo Park, California, in September 2007. Thanks are given to M. Suarez for her careful reading of the manuscript and constructive remarks. G. Sánchez N. and her team at Unidad de Servicios de Información helped us in locating useful references. Partial support from Dirección General de Asuntos del Personal Académico, Universidad Nacional Autónoma de México, Mexico, under Project Number IN114706, is gratefully acknowledged.

References

Aki, K., and P. G. Richards (2002). *Quantitative Seismology*, Second Ed., University Science Books, Sausalito.

Atluri, S. N. (2004). *The Meshless Method (MLPG) for Domain and BIE Discretizations*, Tech. Science Press, Forsyth, Georgia.

Bielak, J., and P. Christiano (1984). On the effective seismic input for nonlinear soil-structure interaction systems, *Earthq. Eng. Struct. Dyn.* **12,** 107–119.

Bouchon, M., and K. Aki (1982). Strain, tilt, and rotation associated with strong ground motion in the vicinity of earthquake faults, *Bull. Seismol. Soc. Am.* **72,** 1717–1738.

Castellani, A., and G. Boffi (1986). Rotational components of the surface ground motion during an earthquake, *Earthq. Eng. Struct. Dyn.* **14,** 751–767.

Cochard, A., H. Igel, B. Schuberth, W. Suryanto, A. Velikoseltsev, U. Schreiber, J. Wassermann, F. Scherbaum, and D. Vollmer (2006). Rotational motions in seismology: theory, observations, simulation, in *Earthquake Source Asymmetry, Structural Media and Rotation Effects*, R. Teisseyre, M. Takeo, and E. Majewski (Editors), Springer-Verlag, New York.

Fairweather, G., and A. Karageorghis (1998). The method of fundamental solutions for elliptic boundary value problems, *Adv. Comp. Math.* **9,** 69–95.

Ghayamghamian, M. R., and G. R. Nouri (2007). On the characteristics of ground motion rotational components using Chiba dense array data, *Earthq. Eng. Struct. Dyn.* **36,** 1407–1429.

Godinho, L., A. Tadeu, and P. Amado Mendes (2007). Wave propagation around thin structures using the MFS, *Comput. Mat. Contin.* **5,** 117–128.

Godinho, L., A. Tadeu, and N. A. Simões (2006). Accuracy of the MFS and BEM on the analysis of acoustic wave propagation and heat conduction problems, in *Advances in Meshless Methods*, Jan Sladek and Vladimir Sladek (Editors), Tech. Science Press, Forsyth, Georgia.

Golberg, M. A., and C. S. Chen (1999). The method of fundamental solutions for potential, Helmholtz and diffusion problems, in *Boundary Integral Methods: Numerical and Mathematical Aspects*, M. A. Golberg (Editor), WIT Press and Computational Mechanics Publications, Boston, 103–176.

Graizer, V. M. (2005). Effect of tilt on strong motion data processing, *Soil Dyn. Earthq. Eng.* **25,** 197–204.

Graizer, V. M. (2006). Tilts in strong ground motion, *Bull. Seismol. Soc. Am.* **96,** no. 6, 2090–2102.

Huang, B. S. (2003). Ground rotational motions of the 1991 Chi-Chi, Taiwan earthquake as inferred from dense array observations, *Geophys. Res. Lett.* **30,** 1307–1310.

Huang, B. S., C. C. Liu, C. R. Lin, C. F. Wu, and W. H. K. Lee (2006). Measuring mid- and near-field rotational ground motions in Taiwan, in a poster presented at the *2006 Fall American Geophysical Union Meeting*, San Francisco.

Joyner, W. B., and D. M. Boore (1993). Methods for regression analysis of strong-motion data, *Bull. Seismol. Soc. Am.* **83,** 469–487.

Kalkan, E., and V. Graizer (2007). Coupled tilt and translational ground motion response spectra, *J. Struct. Eng.* **133,** 609–619.

Kansa, E. J. (1990). A scattered data approximation scheme with applications to computational fluid dynamics II, *Comput. Math. Appl.* **19,** 147–161.

Komatitsch, D., J. P. Jean-Pierre Vilotte, R. Rossana Vai, J. M. Castillo-Covarrubias, and F. J. Sánchez-Sesma (1999). The spectral element method for elastic wave equations: Application to 2D and 3D seismic problems, *Int. J. Num. Meth. Eng.* **45,** 1139–1164.

Komatitsch, D., S. Tsuboi, and J. Tromp (2005). The spectral-element method in seismology, in *Seismic Earth: Array Analysis of Broadband Seismograms*, A. Levander and G. Nolet (Editors), Vol. **157**, American Geophysical Union, Washington, D.C., 205–228.

Lee, V. W., and M. D. Trifunac (1985). Torsional accelerograms, *Int. J. Soil Dyn. Earthq. Eng.* **4,** 132–139.

Lee, V. W., and M. D. Trifunac (1987). Rocking strong earthquake accelerations, *Int. J. Soil Dyn. Earthq. Eng.* **6,** 75–89.

Li, H-N, L-Y Sun, and S-Y Wang (2004). Improved approach for obtaining rotational components of seismic motion, *Nucl. Eng. Des.* **232,** 131–137.

Niazi, M. (1986). Inferred displacements, velocities and rotations of a long rigid foundation located at El Centro differential array site during the 1979 Imperial Valley, California, earthquake, *Earthq. Eng. Struct. Dyn.* **14,** no. 4, 531–542.

Nigbor, R. (1994). Six-degree-of-freedom ground-motion measurement, *Bull. Seismol. Soc. Am.* **84,** 1665–1669.

Oliveira, C. S., and B. A. Bolt (1989). Rotational components of surface strong ground motion, *Earthq. Eng. Struct. Dyn.* **18,** 517–526.

Paolucci, R., E. Faccioli, and F. Maggio (1999). 3D response analysis of an instrumented hill at Matsuzaki, Japan, by a spectral method, *J. Seism.* **3,** 191–209.

Pedersen, H., F. Sánchez-Sesma, and M. F. Campillo (1994). Three-dimensional scattering by two-dimensional topographies, *Bull. Seismol. Soc. Am.* **84,** 1169–1183.

Pillet, R., and J. Virieux. (2007). The effects of seismic rotations on inertial sensors, *Geophys. J. Int.* **171,** no. 3, 1314–1323.

Reinoso, E., L. Wrobel, and H. Power (1997). Three-dimensional scattering of seismic waves from topographical structures, *Soil Dyn. Earthq. Eng.* **16,** 41–61.

Sánchez-Sesma, F. J. (1990). Elementary solutions for the response of a wedge-shaped medium to incident *SH* and *SV* waves, *Bull. Seismol. Soc. Am.* **80,** 737–742.

Sánchez-Sesma, F. J., and M. Campillo (1991). Diffraction of *P*, *SV*, and Rayleigh waves by topographic features: A boundary integral formulation, *Bull. Seismol. Soc. Am.* **81,** no. 6, 2234–2253.

Sánchez-Sesma, F. J., and E. Rosenblueth (1979). Ground motion at canyons of arbitrary shape under incident *SH* waves, *Earthq. Eng. Struct. Dyn.* **7,** 441–450.

Singh, S. K., M. Santoyo, P. Bodin, and J. Gomberg (1997). Dynamic deformations of shallow sediments in the Valley of Mexico, Part II: Single-station estimates, *Bull. Seismol. Soc. Am.* **87,** 540–550.

Spudich, P., and J. B. Fletcher (2008). Observation and prediction of dynamic ground strains, tilts and torsions caused by the *M* 6.0 2004 Parkfield, California, earthquake and aftershocks derived from UPSAR array observations, *Bull. Seismol. Soc. Am.* **98,** no. 4, 1898–1914.

Suryanto, W., H. Igel, J. Wassermann, A. Cochard, B. Schuberth, D. Vollmer, F. Scherbaum, U. Schreiber, and A. Velikoseltsev (2006). First comparison of array-derived rotational ground motions with direct ring laser measurements, *Bull. Seismol. Soc. Am.* **96,** 2059–2071.

Tadeu, A, and E. Kausel (2000). Green's functions for two-and-a-half dimensional elastodynamic problems, *J. Eng. Mech.* **126,** 1093–1097.

Tadeu, A., J. António, and L. Godinho (2001). Green's function for two-and-a-half dimensional elastodynamic problems in a half-space, *Comput. Mech. J.* **27,** 484–491.

Tadeu, A., P. Santos, and J. António (2001). Amplification of elastic waves due to a point source in the presence of complex surface topography, *J. Comp. Struct.* **79,** no. 18 1697–1712.

Takeo, M. (1998). Ground rotational motions recorded in near-source region of earthquakes, *Geophys. Res. Lett.* **25,** 789–792.

Takeo, M., and H. M. Ito (1997). What can be learned from rotational motions excited by earthquakes?, *Geophys. J. Int.* **129,** 319–329.

Trifunac, M. D. (1982). A note on rotational components of earthquake motions on ground surface for incident body waves, *Soil Dyn. Earthq. Eng.* **1,** 11–19.

Trifunac, M. D. (2006). Effects of torsional and rocking excitations on the response of structures, in *Earthquake Source Asymmetry, Structural Media and Rotation Effects*, R. Teisseyre, M. Takeo, and E. Majewski (Editors), Springer-Verlag, New York, 569–582.

Wang, H., H. Igel, A. Cochard, and M. Ewald (2006). Variations of peak ground motions due to slip histories: Application to the Newport Inglewood fault, Los Angeles basin, in *the International Symposium on the Effects of Surface Geology on Seismic Motion*, Vol. 3, Grenoble, France.

Centro de Investigação em Ciências da Construção
Department of Civil Engineering
University of Coimbra
Rua Luis Reis Santos Pólo 2-FCTUC
3030-788 Coimbra, Portugal
lgodinho@dec.uc.pt
pamendes@dec.uc.pt
tadeu@dec.uc.pt
(L.G., P.A., A.T.)

Instituto de Ingeniería
Universidad Nacional Autónoma de México
Ciudad Universitaria, Coyoacán 04510
Mexico, D.F., Mexico
acadenai@ii.unam.mx
sesma@servidor.unam.mx
(A.C., F.J.S.)

ROSE School
c/o EUCENTRE
via Ferrata 1
Pavia 27100, Italy
csmerzini@roseschool.it
(C.S.)

Laboratoire de Modélisation et d'Imagerie en Géosciences de Pau (CNRS)
UMR 5212
Université de Pau et des Pays de l'Adour and INRIA MAGIQUE-3D
Bâtiment IPRA
Avenue de l'Université
BP 1155, 64013 Pau Cedex, France
ronan.madec@gmail.com
dimitri.komatitsch@univ-pau.fr
(R.M., D.K.)

Manuscript received 31 May 2008